

Article

Observation of Wavelength Tuning in a Mode-Locked Figure-9 Fiber Laser

Han Zhang ^{1,2}, Handing Xia ^{1,*} , Mengqiu Fan ¹ , Junwen Zheng ¹, Jianbin Li ¹, Xiaocheng Tian ¹, Dandan Zhou ¹, Zhimeng Huang ¹, Fan Zhang ¹, Rui Zhang ¹, Zhitao Peng ¹ and Qihua Zhu ^{1,*}

¹ Research Center of Laser Fusion, China Academy of Engineering Physics, Mianyang 621900, China

² Graduate School of China Academy of Engineering Physics, Beijing 100088, China

* Correspondence: qihzh@163.com (Q.Z.); hdxia2008@sina.com (H.X.)

Abstract: We demonstrate an all-PM Er-doped soliton mode-locked fiber oscillator based on the figure-9 configuration with a compact adjustable reflection-type non-reciprocal phase shifter. An analytical model based on the Jones matrix is established to simulate the wavelength tuning phenomenon. Experimentally, it is observed that the increase in pump power results in a significant redshift in the spectrum of output pulses. When the angle of the half-wave plate is rotated in one direction, the output spectrum is redshifted and then blueshifted successively. Good qualitative agreement is presented between the simulations and the experimental results. It is shown that the increase in pump power changes the nonlinear phase shift, which causes the redshift of the transmittance curves at the laser output port. In contrast, the rotation of wave plates not only changes the nonlinear phase shift difference, but also causes variations in linear phase bias and modulation depth. The changes in these parameters lead to the redshift and blueshift of the transmission curves, which enables wavelength tuning.

Keywords: ultrafast laser; figure-9 mode-locked fiber laser; NALM; wavelength tuning



Citation: Zhang, H.; Xia, H.; Fan, M.; Zheng, J.; Li, J.; Tian, X.; Zhou, D.; Huang, Z.; Zhang, F.; Zhang, R.; et al. Observation of Wavelength Tuning in a Mode-Locked Figure-9 Fiber Laser. *Photonics* **2023**, *10*, 184. <https://doi.org/10.3390/photonics10020184>

Received: 5 January 2023

Revised: 31 January 2023

Accepted: 6 February 2023

Published: 8 February 2023



Copyright: © 2023 by the authors. Licensee MDPI, Basel, Switzerland. This article is an open access article distributed under the terms and conditions of the Creative Commons Attribution (CC BY) license (<https://creativecommons.org/licenses/by/4.0/>).

1. Introduction

Ultrashort-pulse mode-locked fiber lasers have attracted extensive attention owing to their potential applications in the fields of high-precision micro-machining, nonlinear optics and biological imaging, etc. [1–5]. The robustness and reliability of ultrafast fiber lasers is affected by the mode locking technique. Generally, two main categories of mode locking methods are widely employed to realize the generation of ultrashort pulses in fiber lasers. One type refers to the real saturable absorbers (SAs), such as semiconductor saturable absorber mirrors (SESAM) [6], novel two-dimensional materials [7–9] and oxide saturable absorbers [10]. The other category refers to artificial saturable absorbers including nonlinear polarization rotation (NPR) [11–14] and nonlinear amplifying loop mirrors (NALM) [15–19]. However, real SAs may suffer from a low damage threshold and potential degradation over time [20]. Normally, the cavity of an NPR mode-locked fiber laser cannot be constructed using polarization-maintaining (PM) fiber, which limits its application in unstable conditions. Although many efforts have been made to realize NPR with an all-fiber and all-PM structure [21,22], it requires splicing the PM fiber at the proper angle or using other optimization methods, which inevitably adds complexity and extra losses in the cavity.

Compared with real SAs and conventional NPR methods, fiber lasers mode-locked by the NALM technique are more robust due to their all-PM configuration and the abandonment of real SAs. The mode locking mechanism of NALM relies on the interference between two counter-propagating pulses inside a fiber loop connected by a beam splitter. One drawback of NALM mode-locked fiber lasers, e.g., figure-8 fiber lasers [23], is the difficulty in self-starting, due to the weak intensity dependence caused by the phase difference between the clockwise (*cw*) and counterclockwise (*ccw*) propagating pulses. Therefore,

more robust mode locking techniques with better self-start performance are desirable. Recently, figure-9 fiber lasers based on phase-biased NALM configuration have attracted great interest due to the artful modification of the laser cavity so that the mode locking is self-started easily [16]. Specifically, an additional linear phase bias is introduced in the ring mirror or linear arm of the figure-9 cavity. Thanks to the extra phase bias, the transmission level of the running continuous wave (CW) as well as the noise pulse increases at the laser starting point. Therefore, the mode locking threshold is reduced and the self-starting becomes easier compared to NALM fiber lasers without linear phase bias [16,23]. Commonly, the phase biasing module consists of a set of wave plates and Faraday rotators [24,25]. If the phase shifter is composed of several adjustable space optical wave plates, both the phase bias and modulation depth can be adjusted by rotating the wave plate angle, so that the tunable structure can have more freedom in the emitting pulses' optimization. It has been shown that the figure-9 fiber lasers based on the NALM configuration not only generate optical pulses with a narrow pulse width, high repetition rate and ultra-low noise and time jitter level [26–28], but also have very high robustness to meet the application conditions in extreme environments [29]. Although there have been many previous studies on the properties of figure-9 fiber lasers reported so far, their wavelength tuning properties are rarely reported. The influence of the cavity parameters (e.g., phase shift and pump power) on the wavelength tuning outcomes has not been observed, and the mechanism of wavelength tuning remains to be explored.

In this work, we demonstrate an all-PM Er-doped soliton mode-locked fiber oscillator based on the figure-9 configuration. A compact reflection-type non-reciprocal phase shifter is implemented for reducing the mode-locking threshold of the laser. An analytical model based on the Jones matrix is established to qualitatively simulate the wavelength tuning phenomenon. It is observed that the increase in pump power results in a significant redshift in the spectrum of output pulses. As the angle of the half-wave plate is rotated in one direction, the output spectrum is redshifted and then blueshifted successively. The simulated results are well validated by the experiments. It is shown that the adjustment of pump power causes the change in the nonlinear phase shift difference of the NALM. The angle rotation of wave plates not only changes the nonlinear phase shift difference, but also causes a difference in laser phase bias and modulation depth. The change in these parameters leads to a difference in the distribution of the laser output transmission curves, which results in wavelength tuning. This work provides a new perspective for the design of continuously tunable mode-locked figure-9 fiber lasers and the expansion of their applications.

2. Experimental Setup and Theoretical Analysis

A schematic illustration of the figure-9 fiber oscillator is shown in Figure 1. The cavity consists of two modules, the NALM segment and a linear arm. The NALM is composed of a polarization beam combiner integrated with a collimation lens (Col-PBC), a PM wavelength division multiplexer (WDM), 0.6 m of PM erbium-doped fiber (PM-EDF, Er80-8/125-PM) with anomalous dispersion of $-0.023 \text{ ps}^2/\text{m}$ and 3.25 m of PM single-mode fiber (PM1550) with dispersion of $-0.023 \text{ ps}^2/\text{m}$. The PM-EDF, with $\sim 80 \text{ dB/m}$ absorption at 1530 nm, is used as the gain medium. In order to increase the nonlinear phase shift difference between the two counter-propagating pulses, the PM-EDF is placed asymmetrically in the fiber loop and pumped by a 976 nm laser diode (LD) through the WDM, which facilitates the self-starting of mode locking. In particular, there are 0.7 m and 2.55 m of the PM1550 on the front and back sides of the PM-EDF along the *ccw* direction, respectively. By passing through the PBS at the end of the NALM fiber loop, the polarization of pulses from the *cw* and *ccw* directions is twisted by a 90° angle. Then, they are combined and coupled into the linear arm through the Col-PBC. The two combined beams with orthogonal polarizations from the collimator pass through a non-reciprocal phase shifter consisting of a 45° Faraday rotator (FR), a half-wave plate (HWP) and a quarter-wave plate (QWP). The linear phase shift can be adjusted by rotating these two wave plates. A polarization beam splitter (PBS)

is placed behind the phase shifter. Then, coherent polarization interference between the two combined beams occurs at the PBS, resulting in intensity-dependent transmission characteristics at both ports. The peak part of the pulse is more powerful; thus, it is easier to achieve a large phase difference and thus has higher transmittance. The two wings of the pulse are reflected due to the weak light intensity and insufficient phase shift. This process forms the pulse narrowing mechanism, or an artificial “saturable absorber”. The *p*-polarized light, transmitted from the PBS, is 90% reflected back and 10% coupled to the output port 1 via a 90% reflected end-mirror on the linear arm. The rejected part of the light (*s*-polarized) is coupled out to output 2 from the PBS. The linear arm is integrated in a compact box with a size of $90 \times 50 \times 40 \text{ mm}^3$. The physical length of the linear arm is only $\sim 7.5 \text{ cm}$. The total optical path length of the laser is 5.77 m, and the corresponding pulse repetition rate is 52 MHz. The net cavity dispersion is estimated to be approximately -0.09 ps^2 .

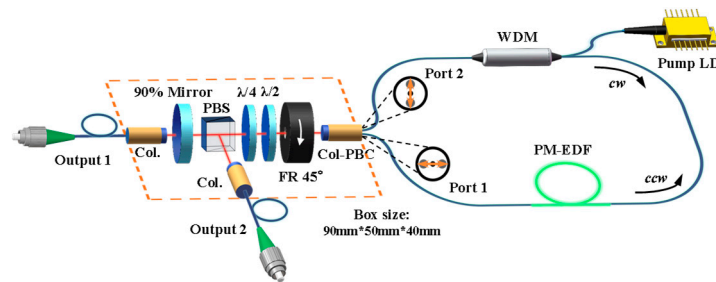


Figure 1. Configuration of the figure-9 mode-locked fiber laser. PBS: polarization beam splitter; $\lambda/4$: quarter-wave plate; $\lambda/2$: half-wave plate; FR: Faraday rotator; Col-PBC: polarization beam combiner integrated with collimation lens; WDM: wavelength division multiplexer; PM-EDF: polarization-maintaining erbium-doped fiber; LD: laser diode; *cw*: clockwise; *ccw*: counter-clockwise.

According to the cavity setup shown in Figure 1, we deduce the cavity roundtrip transmission function. It is assumed that the light passes through the PBS, QWP, HWP, FR, Col-PBC, and NALM. Then, the light returns by the same route to the PBS. In particular, the intracavity elements are expressed by their corresponding Jones matrices [30]. Thus, the intracavity electric field, \vec{E}_{output1} , after one roundtrip is obtained:

$$\vec{E}_{\text{output1}}(\theta_h, \theta_q, \Delta\varphi_{nl}) = M_{\text{PBS, trans}} M_{\text{QWP}}(\theta_q) M_{\text{HWP}}(\theta_h) M_{\text{FR}}(45^\circ) M_{\text{loop}} M_{\text{nl}}(\Delta\varphi_{nl}) M_{\text{FR}}(45^\circ) M_{\text{HWP}}(\theta_h) M_{\text{QWP}}(\theta_q) \vec{e}_x \quad (1)$$

where $\vec{e}_x = (1, 0)$ is the normalized field vector along the *x*-axis, i.e., corresponding to the *p*-polarized light transmitted from the PBS. The other terms in Equation (1) are the Jones matrices of the corresponding components in the resonator, where $M_{\text{PBS, trans}}$ is the Jones matrix of the transmittance of PBS. M_{loop} is the Jones matrix of light transmission through the fiber loop of NALM. $M_{\text{nl}}(\Delta\varphi_{nl})$ represents the nonlinear phase shift difference accumulated after the light passes through the fiber loop. θ_h and θ_q are the fast-axis angles of HWP and QWP, respectively. $\Delta\varphi_{nl}$ is the nonlinear phase difference between the *ccw* and *cw* light. Then, the cavity roundtrip transmission function *T* corresponds to

$$T(\theta_h, \theta_q, \Delta\varphi_{nl}) = \left| \vec{E}_{\text{output1}} \right|^2 \quad (2)$$

which can be simplified as

$$T(\theta_h, \theta_q, \Delta\varphi_{nl}) = \frac{1}{2}(1 + \cos \Delta\varphi_{nl}) [\sin^2(4\theta_h - 2\theta_q) + \cos^2(4\theta_h - 2\theta_q) \sin^2(2\theta_q)] + \cos^2(2\theta_q) \sin^2(\Delta\varphi_{nl}/2) - \frac{1}{2} \cos(4\theta_h - 2\theta_q) \sin(4\theta_q) \sin \Delta\varphi_{nl} \quad (3)$$

where $\Delta\varphi_{nl} = \varphi_{nl}^{ccw} - \varphi_{nl}^{cw}$ can be obtained by calculating the following formula [31]:

$$\varphi_{nl}^{ccw} = \frac{\pi}{\lambda_s A_{eff}} n_2 P_0 \alpha \left(L_1 + \frac{g_1 - 1}{\ln g_1} L_2 + g_1 L_3 \right) \tag{4}$$

$$\varphi_{nl}^{cw} = \frac{\pi}{\lambda_s A_{eff}} n_2 P_0 (1 - \alpha) \left(g_2 L_1 + \frac{g_2 - 1}{\ln g_2} L_2 + L_3 \right) \tag{5}$$

$$\Delta\varphi_{nl} = \frac{\pi n_2 P_0}{\lambda_s A_{eff}} \left\{ [\alpha - (1 - \alpha)g_2]L_1 + \left[\alpha \frac{g_1 - 1}{\ln g_1} - (1 - \alpha) \frac{g_2 - 1}{\ln g_2} \right] L_2 + (\alpha g_1 - 1 + \alpha)L_3 \right\} \tag{6}$$

where φ_{nl}^{cw} and φ_{nl}^{ccw} are the nonlinear phase shifts accumulated in the NALM by the *ccw* and *ccw* transmitting optical fields. g_1 and g_2 are the gains of *ccw* and *ccw* propagating light in NALM, respectively. P_0 is the peak power of the pulse incident into the NALM. n_2 is the nonlinear refractive index of the fiber. L_2 is the length of EDF (0.6 m), and α is the energy splitting ratio coupled into port 1 at the loop entrance. Obviously, the value of $\Delta\varphi_{nl}$ can be either positive or negative, and its absolute value is jointly determined by the peak power P_0 , the splitting ratio α and the asymmetry of NALM. The splitting ratio α is defined as

$$\alpha = |E_{port\ 1}|^2 \tag{7}$$

The normalized field vector at the entrance of the loop can be expressed as

$$\vec{E}_{port\ 1} = M_{FR}(45^\circ) M_{HWP}(\theta_h) M_{QWP}(\theta_q) \vec{e}_x \tag{8}$$

From Equation (3) above, it is deduced that different combinations of θ_q and θ_h result in different roundtrip transmissions in the cavity. The simulation results of the cavity roundtrip transmission function T are presented in Figure 2. As shown in Figure 2a, when θ_q is 0° (that is, the fast axis of the QWP is parallel to the x-axis), adjusting θ_h only changes the modulation depth, and not the linear phase bias. It is difficult to achieve self-starting operation in these states because small deviations of $\Delta\varphi_{nl}$ from zero only lead to small changes in the cavity losses. There is another special case of $\theta_q = 45^\circ$, where the incident, linearly polarized light is converted to circularly polarized light after passing through QWP. At this time, the light coupled to Col-PBC remains circularly polarized as the HWP is rotated. The optical splitting ratio α of NALM continues to be 0.5. In this case, the maximum transmission is obtained at the point of $\Delta\varphi_{nl} = 0$. This indicates that the laser exhibits decreasing transmission as a function of $\Delta\varphi_{nl}$ and the laser works in the region of negative saturation absorption, resulting in difficult self-starting operation. When θ_q is not 0° and is not an integer multiple of 45° , adjusting θ_h changes both the modulation depth and the linear phase bias. As shown in Figure 2b, when θ_q is set to 13.5° , the transmission curves have different modulation depths and linear phase biases when tuning θ_h . In this case, due to the introduced phase bias, the transmittance curves have a steeper slope around $\Delta\varphi_{nl} = 0$ than that of the cases in Figure 2a, which means that the transmittance increases more quickly when increasing the pump power. Moreover, the linear phase bias results in partial CW transmission in the initial phase of pulse formation (corresponding to $\Delta\varphi_{nl} = 0$), which helps to generate the initial noise-like giant pulses required for mode locking and to enhance the self-starting ability of the mode locking. Theoretically, it can be defined that the value range, where the pulse transmittance is greater than the CW component, is the region of single-pulse mode locking operation [32].

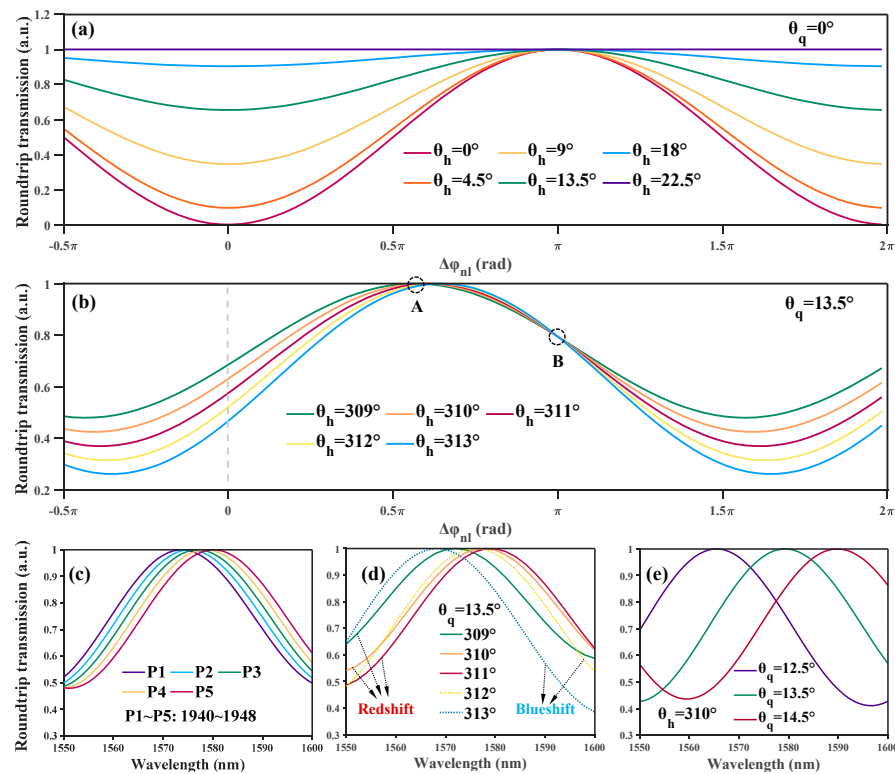


Figure 2. Simulation results. (a) $\theta_q = 0^\circ$, the transmittance curves when tuning θ_h ; (b) $\theta_q = 13.5^\circ$, the transmittance curves when tuning θ_h ; (c) $\theta_q = 13.5^\circ$, $\theta_h = 310^\circ$, simulation spectra when increasing the value of P_0 ; (d) $\theta_q = 13.5^\circ$, simulation spectra when tuning θ_h ; (e) $\theta_h = 310^\circ$, simulation spectra when tuning θ_q .

According to Equations (3) and (6), the transmittance curves as a function of wavelength are qualitatively simulated. For the case of $\theta_q = 13.5^\circ$ and $\theta_h = 310^\circ$, as the pump power increases from P_1 to P_5 , the spectrum of the output pulses is redshifted, as shown in Figure 2c. Furthermore, the wavelength tuning induced by rotating θ_h is simulated, as shown in Figure 2d. Interestingly, the phenomenon of non-unidirectional spectral tuning is observed with the unidirectional change of θ_h . By increasing the angle of θ_h , the transmission curve with the wavelength of port 1 is first redshifted and then blueshifted successively. This is because different θ_h leads to different transmittance curve distributions. Similarly, the simulation of the transmission spectrum change caused by rotation θ_q is shown in Figure 2e. We note that the increase in θ_q leads to a spectral redshift. A small change in θ_q leads to a relatively larger step of wavelength tuning compared to adjusting θ_h . Therefore, it is numerically shown that the wavelength tuning in our proposed laser cavity is strongly correlated to the pulse peak power (namely, the nonlinear phase shift) and the angle combinations of wave plates.

3. Experiment Results and Discussion

Once the angles of QWP and HWP are adjusted to the appropriate position, the self-started mode locking operation can be achieved by increasing the pump power of LD to the level of 250 mW. Compared with the traditional figure-8 mode-locked oscillator without a phase shifter [33], the mode-locked threshold is significantly reduced, and no additional mechanical disturbance is required to trigger the self-starting of mode locking. Experimentally, there is a series of angle combinations of wave plates in the whole parameter space of the figure-9 cavity laser to achieve mode-locked pulses. Inspired by the simulation results shown in Figure 2, the angles of QWP and HWP are set to be $\theta_q = 15^\circ$ and $\theta_h = 328^\circ$, respectively. We note that there are minor differences in the angles of the wave plates between the experiment and the simulation, which is due to the angle errors

in the installation of the PBS, the wave plates and the polarizer integrated in Col-PBC. Initially, the laser operates in a multi-pulse soliton mode locking state. By decreasing the pump power below 78 mW, the single-pulse operation is obtained. The minimum pump power level to maintain the laser mode locking is 63 mW. The mode locking performance at the pump power of 65 mW is shown in Figure 3. The spectral characteristics of both output ports are recorded via an optical spectrum analyzer with a wavelength resolution of 0.02 nm, as presented in Figure 3a,c. The full widths at half maximum (FWHM) of the optical spectra are 7.4 nm and 27.6 nm for output 1 and output 2, respectively. The output pulses are conventional soliton pulses because of the typical characteristic Kelly sidebands on both sides of the spectra. Figure 3b,d show the autocorrelation traces of output 1 and output 2 measured by an optical autocorrelator (measurable wavelength range: 1000~1600 nm). When assuming a Sech^2 pulse profile, the corresponding pulse durations are ~360 fs and ~1.26 ps, respectively. The repetition rate of the pulse train is 52 MHz, recorded by a digital oscilloscope with 1 GHz bandwidth, corresponding to a pulse interval of approximately 19.2 ns, as indicated in Figure 3e. Moreover, Figure 3f shows the radio frequency (RF) spectrum of the first harmonic of the transmission port measured by an RF spectrum analyzer. The corresponding signal-to-noise ratio (SNR) is as high as 75 dB with a resolution bandwidth (RBW) of 200 Hz, which indicates the low-amplitude fluctuation and stable operating state of the mode locking.

It is worth noting that the output characteristics of the transmission port (output 1) and rejection port (output 2) are clearly different in both spectral and temporal domains. The pulses emitting from the transmission port have a soliton-type spectrum and a near-perfect Sech^2 pulse shape, as shown in Figure 3a,b. In contrast, the optical spectra of the pulses at the rejection port are noticeably modulated. This is because the backpropagated pulses experience different nonlinear phase shifts due to the gain asymmetry of the NALM segment, so that their temporal and spectral shapes contrast each other when interference occurs [34,35]. Since there is a reflecting end mirror at the transmission port, as the pulse evolves in the cavity, the phase shift accumulated by the pulse transmission in NALM is selected to positively affect the increase in the peak power of the pulse at the transmission port due to the saturable absorption effect. Meanwhile, the rejection port consists of radiation affected by destructive interference, resulting in spectrum sag and poor pulse quality. In the following experiments, we focus on the case of transport ports.

By adding a 1.0-m-length dispersion-compensating fiber (DCF, PM2000D) into the cavity and adjusting the length of the PM1550 fiber appropriately for further dispersion management, the laser is in the state of stretch pulse mode-locked when the net dispersion of the cavity is near-zero micro-negative. In this case, the center wavelength of the spectrum of output 1 is at 1565 nm with an FWHM of 37.4 nm, as shown in Figure 4a. The output pulses with slightly negative chirp are compressed by a piece of PM2000D fiber. The autocorrelation trace of the de-chirped pulses with a pulse duration of 142 fs is shown in Figure 4b, which has a near-perfect Gaussian-function shape. The time bandwidth product (TBP) is 0.65. According to the FWHM of the spectrum, the Fourier transform limited pulse duration is 96 fs. This indicates that there are still some high-order dispersions in the laser cavity that are difficult to compress by DCF. It is worth mentioning that when the laser is operating in the stretch pulse mode-locked state, the spectrum is greatly broadened due to the high peak power of the pulses in the cavity. Due to the relatively larger nonlinear phase shift compared with soliton pulses, the stretched pulses are more easily destroyed during the rotation of the wave plates. Therefore, we prefer the conventional soliton mode locking region to verify the above simulation results in the experiments, where the wavelength tuning characteristics are more obvious.

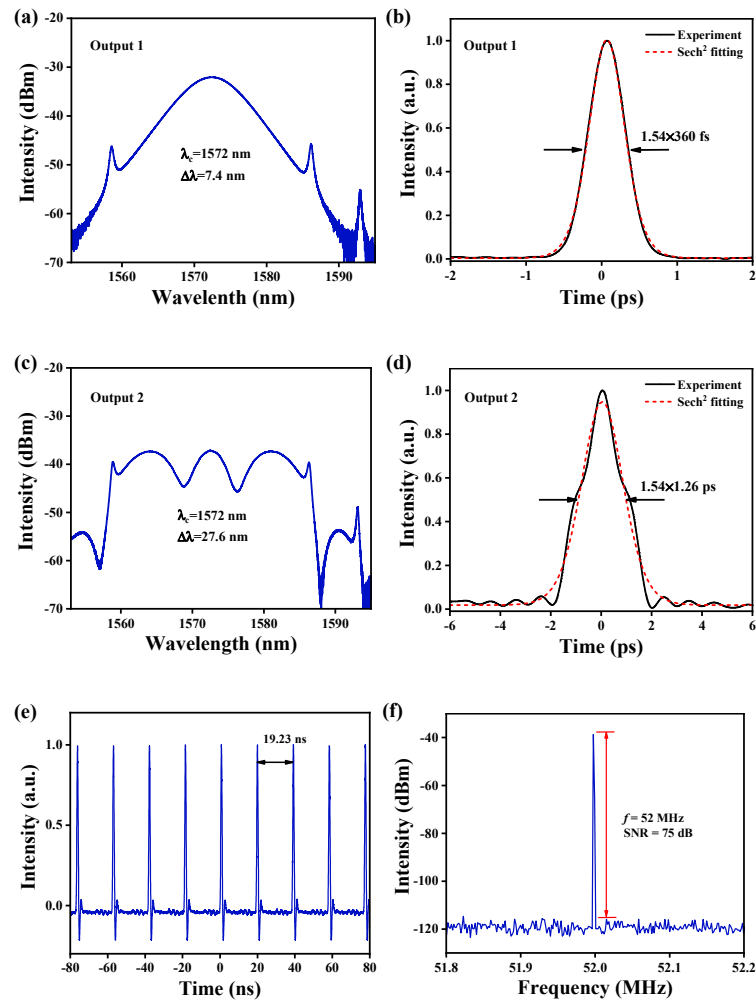


Figure 3. Mode locking performance of the Er-doped figure-9 fiber laser in the conventional soliton mode-locked regime. (a) The optical spectrum at output 1; (b) the autocorrelation trace of direct output pulses (black solid line) and Sech^2 fitting (red dashed line) at output 1; (c) the optical spectrum at output 2; (d) the autocorrelation trace of direct output pulses (black solid line) and Sech^2 fitting (red dashed line) at output 2; (e) the time domain pulse train; (f) the RF spectrum of the first harmonic.

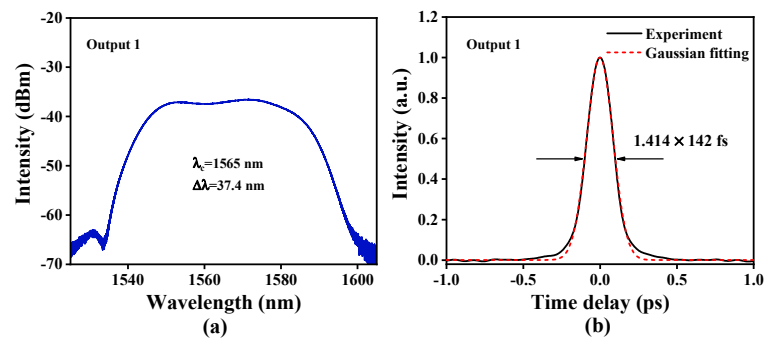


Figure 4. Mode locking performance of the Er-doped figure-9 fiber laser in the stretch pulse mode-locked regime. (a) The output optical spectrum at output 1; (b) the autocorrelation trace of direct output pulses (black solid line) and Gaussian fitting (red dashed line) at output 1.

When the pump power is gradually increased from 65 mW to 78 mW, it is observed that the spectrum of the output pulses is redshifted, as shown in Figure 5a. The central wavelength of the output spectrum is tunable from 1572 nm to 1577 nm. The reason for the pump-induced wavelength tuning is that the increase in pump intensity leads to an

increase in the nonlinear phase shift difference, which causes the transmittance curves about the wavelength to move to the long-wave direction. The experimental results are in good agreement with the above simulation results shown in Figure 2c. Figure 5b presents the central wavelength and FWHM of the main spectral peak as a function of pump power. We note that the FWHM increases monotonically with the rising pump power, due to the self-phase modulation effect [26]. It should be emphasized that when the pump power is increased to 78 mW, an obvious CW component appears on the spectrum, overlapping with the left-side first-order Kelly sideband. Continuing to increase the pump results in more CW components of the spectrum and a smaller redshift step in the spectrum. This can be explained as follows. As the $\Delta\varphi_{nl}$ of NALM increases, the laser operating point gradually shifts from point A, with large transmittance, to point B, with small pulse transmittance, as shown in Figure 2b. Therefore, more of the light wave is output in the form of the CW component.

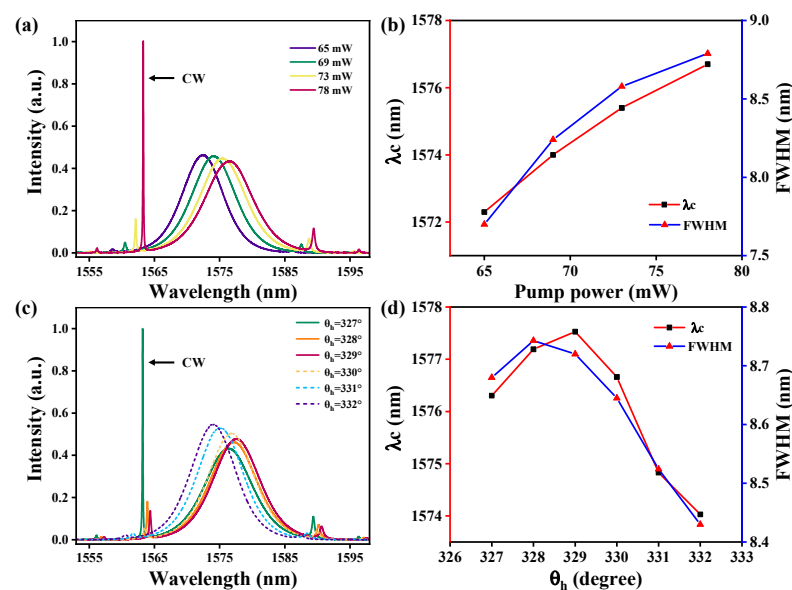


Figure 5. (a) The variation in the output spectra due to increasing pump power; (b) inset: the central wavelength of the spectra and the FWHM of the main spectral peak as a function of pump power; (c) the variation in the output spectra when tuning θ_h ; (d) the central wavelength of the spectra and the FWHM of the main spectral peak as a function of θ_h .

The wavelength tuning triggered by rotating the HWP is shown in Figure 5c for the case in which the pump power is kept at 75 mW. In the tuning range of 327° to 332° , gradually increasing θ_h results in continuous wavelength tuning. The spectrum is first redshifted and then blueshifted, and the tuning range of the central wavelength is 1574 nm to 1577.5 nm. The experimental wavelength tuning phenomenon agrees well with the simulation results in Figure 2d above. The reason for this wavelength tuning phenomenon is that the change in θ_h leads to the different transmittance curve distribution of the output pulses. Figure 5d presents the variation in the FWHM and central wavelength of the main spectral peak of the pulse when θ_h is adjusted. It is thus evident that the FWHM has the same variation trend as the central wavelength. This demonstrates that adjusting θ_h not only causes the wavelength shift of the laser output transmission curve, but also leads to the spectral bandwidth change. The longer spectral wavelength corresponds to a larger FWHM. It should be pointed out that when θ_h decreases to 327° , the CW component begins to appear in the spectrum, as shown in Figure 5c. The reason is as follows.

The laser works in the negative saturation absorption region when the pump power is greater than 65 mW, as shown in Figure 5a. When the pump power is kept at 75 mW, the main spectral peak of the intracavity pulse decreases when reducing the θ_h . This indicates that the output transmission of the laser pulse light becomes smaller, i.e., the nonlinear

phase shift difference increases. Moreover, the transmittance of the CW is located at the point of $\Delta\varphi_{nl} = 0$. According to the simulation results in Figure 2b, the smaller the θ_h is, the larger transmittance the CW has. Therefore, the CW component appears on the spectrum of the output pulse when θ_h decreases.

Experimentally, the laser fails to maintain the mode locking state when θ_h is less than 325° . This could be attributed to the fact that the nonlinear phase shift difference of the NALM exceeds the range that allows stable single-pulse mode locking. Moreover, the laser also cannot maintain mode-locked operation when θ_h is greater than 332° . The reason is clarified as follows. The main spectral peak increases with an increasing θ_h , which indicates that the output transmittance of the laser increases—that is, the nonlinear phase shift difference decreases. The transmittance of pulse light reaches its maximum value when $\theta_h = 332^\circ$. The continuing increase in θ_h leads to a smaller nonlinear phase shift difference and causes the laser to work in a negative saturated absorption state, which makes it difficult for the laser to maintain stable mode locking.

In addition, the Kelly sideband strength is also related to the rotation of HWP. As shown in Figure 5c, the Kelly sidebands of the output spectrum are gradually suppressed when θ_h is tuned from 327° to 332° . This phenomenon is similar to the situation of the pump power decreasing process, as shown in Figure 5a. This indicates that the Kelly sideband strength depends not only on the pump strength but also on the nonlinear phase shift difference. The reduction of the nonlinear phase shift difference helps to suppress the Kelly sideband strength. Different from the situation in Figure 5a, increasing θ_h causes the laser to operate with larger pulse transmittance at higher pump power, which leads to a significant increase in the spectral energy of the output pulse, as shown in Figure 5c. It is worth pointing out that based on this property, it is possible to increase the pulse energy while greatly suppressing the Kelly sideband strength by rotating HWP.

For the case of adjusting θ_q , as expected from the simulation results in Figure 2e, an increase in θ_q does lead to a redshift in the wavelength. However, the mode-locked state of the laser is very sensitive to the change in θ_q . The slight rotation of the QWP causes the laser to fail to maintain mode locking operation. This is due to the uneven shape of the Er^{3+} ions' emission spectrum [36]. When adjusting θ_q , it results in a large step shift in the spectrum, and the energy balance of the mode-locked state is easily destroyed due to drastic changes in the gain or loss of the pulses in the cavity.

The total wavelength tuning range for our experiments is 3.5~5 nm. We believe that by further nonlinear optimization and more detailed adjustment of the combination of wave plate angles, tunable pulses output in a wider spectral range can be obtained. Additionally, the figure-9 fiber laser introduced in this work is capable of continuous wavelength tuning without the aid of additional tunable optical bandpass filters [37] or other wavelength tuning components, compared to traditional fiber lasers based on real SAs. It has important application value in optical fiber communication, optical fiber sensing, biological imaging and other fields.

4. Conclusions

In conclusion, we demonstrated a 52 MHz all-PM Er-doped soliton mode-locked fiber oscillator based on the figure-9 configuration, in which we developed a compact reflection-type non-reciprocal phase shifter for reducing the mode locking threshold of the laser. An analytical model based on the Jones matrix is established to simulate the wavelength tuning phenomenon induced by adjusting the pump power level and wave plate angle in the figure-9 fiber oscillator. The experimental results reveal that an increase in pump power leads to a significant redshift in the spectral output of the pulses. Furthermore, the experiments demonstrate that rotating the angle of the half-wave plate in one direction causes the output spectrum to undergo successive redshifting and blueshifting. The simulation results are well verified by experiments. It is shown that the increase in pump power results in a change in the nonlinear phase shift, which in turn leads to a redshift in the transmittance curves at the laser output port. On the other hand, rotating the wave plates not only alters

the nonlinear phase shift difference, but also causes variations in the linear phase bias and modulation depth, which ultimately results in the redshift and blueshift of the transmission curves, thereby enabling wavelength tuning. This work provides a new perspective for the design of tunable mode-locked figure-9 fiber lasers and the expansion of their applications.

Author Contributions: Conceptualization, H.Z. and H.X.; methodology, H.Z. and H.X.; software, H.Z. and H.X.; validation, M.F., J.L., J.Z., X.T., D.Z., Z.H. and F.Z.; formal analysis, H.Z.; investigation, H.Z. and H.X.; resources, H.X.; data curation, H.Z.; writing—original draft preparation, H.Z.; writing—review and editing, H.X. and Q.Z.; visualization, H.Z.; supervision, R.Z., Z.P. and Q.Z.; project administration, H.X., R.Z., Z.P. and Q.Z.; funding acquisition, H.X. All authors have read and agreed to the published version of the manuscript.

Funding: This research was funded by the National Natural Science Foundation of China (11904339, 62075201).

Institutional Review Board Statement: Not applicable.

Informed Consent Statement: Not applicable.

Data Availability Statement: The datasets generated for this study are available on request to the corresponding author.

Conflicts of Interest: The authors declare no conflict of interest.

References

1. Fermann, M.E.; Hartl, I. Ultrafast fibre lasers. *Nat. Photonics* **2013**, *7*, 868–874. [[CrossRef](#)]
2. Jauregui, C.; Limpert, J.; Tünnermann, A. High-power fibre lasers. *Nat. Photonics* **2013**, *7*, 861–867.
3. Kerse, C.; Kalaycıoğlu, H.; Elahi, P.; Cetin, B.; Kesim, D.; Akcaalan, O.; Yavas, S.; Asik, M.; Oktem, B.; Hoogland, H.; et al. Ablation-cooled material removal with ultrafast bursts of pulses. *Nature* **2016**, *537*, 84–88. [[PubMed](#)]
4. Cundiff, S.T.; Weiner, A.M. Optical arbitrary waveform generation. *Nat. Photonics* **2010**, *4*, 760–766. [[CrossRef](#)]
5. Nishizawa, N. Ultrashort pulse fiber lasers and their applications. *Jpn. J. Appl. Phys.* **2014**, *53*, 090101. [[CrossRef](#)]
6. Lecourt, J.B.; Duterte, C.; Narbonneau, F.; Kinet, D.; Hernandez, Y.; Giannone, D. All-normal dispersion, all-fibered PM laser mode-locked by SESAM. *Opt. Express* **2012**, *20*, 11918–11923.
7. Sobon, G.; Sotor, J.; Abramski, K.M. All-polarization maintaining femtosecond Er-doped fiber laser mode-locked by graphene saturable absorber. *Laser Phys. Lett.* **2012**, *9*, 581. [[CrossRef](#)]
8. Sobon, G. Mode-locking of fiber lasers using novel two-dimensional nanomaterials: Graphene and topological insulators. *Photonics Res.* **2015**, *3*, A56–A63.
9. Li, L.; Pang, L.; Wang, R.; Zhang, X.; Hui, Z.; Han, D.; Zhao, F.; Liu, W. Ternary transition metal dichalcogenides for high power vector dissipative soliton ultrafast fiber laser. *Laser Photonics Rev.* **2022**, *16*, 2100255. [[CrossRef](#)]
10. Hou, S.; Ma, Z.; Yang, J.; Zhang, M.; Yan, P.; Ruan, S. Mode-locked Er-doped fiber laser based on function-integrated fiber coupler. *Opt. Lett.* **2021**, *46*, 5934–5937.
11. Mortag, D.; Wandt, D.; Morgner, U.; Kracht, D.; Neumann, J. Sub-80-fs pulses from an all-fiber-integrated dissipative-soliton laser at 1 μm . *Opt. Express* **2011**, *19*, 546–551. [[CrossRef](#)] [[PubMed](#)]
12. Chong, A.; Buckley, J.; Renninger, W.; Wise, F. All-normal-dispersion femtosecond fiber laser. *Opt. Express* **2016**, *14*, 10095–10100.
13. Oktem, B.; Ülgüdür, C.; Ilday, F.Ö. Soliton–similariton fibre laser. *Nat. Photonics* **2010**, *4*, 307–311. [[CrossRef](#)]
14. Kong, L.J.; Xiao, X.S.; Yang, C.X. Low-repetition-rate all-fiber all-normal-dispersion Yb-doped mode-locked fiber laser. *Laser Phys. Lett.* **2010**, *7*, 359–362.
15. Fermann, M.E.; Haberl, F.; Hofer, M.; Hochreiter, H. Nonlinear amplifying loop mirror. *Opt. Lett.* **1990**, *15*, 752–754. [[PubMed](#)]
16. Hänsel, W.; Hoogland, H.; Giunta, M.; Schmid, S.; Steinmetz, T.; Doubek, R.; Mayer, P.; Dobner, S.; Cleff, C.; Fischer, M.; et al. All polarization-maintaining fiber laser architecture for robust femtosecond pulse generation. *Appl. Phys. B* **2017**, *123*, 41. [[CrossRef](#)]
17. Agueraray, C.; Hawker, R.; Runge, A.F.; Erkintalo, M.; Broderick, N.G. 120 fs, 4.2 nJ pulses from an all-normal-dispersion, polarization-maintaining, fiber laser. *Appl. Phys. Lett.* **2013**, *103*, 121111. [[CrossRef](#)]
18. Yu, Y.; Teng, H.; Wang, H.B.; Wang, L.N.; Zhu, J.F.; Fang, S.B.; Chang, G.Q.; Wang, J.L.; Wei, Z.Y. Highly-stable mode-locked PM Yb-fiber laser with 10 nJ in 93-fs at 6 MHz using NALM. *Opt. Express* **2018**, *26*, 10428–10434. [[CrossRef](#)]
19. Gao, W.L.; Liu, G.Y.; Zhang, Z.G. 44.6 fs pulses from a 257 MHz Er: Fiber laser mode-locked by biased NALM. *Chin. Opt. Lett.* **2018**, *16*, 111401.
20. Kieu, K.; Wise, F.W. All-fiber normal-dispersion femtosecond laser. *Opt. Express* **2008**, *16*, 11453–11458.
21. Fermann, M.E.; Andrejco, M.J.; Silberberg, Y.; Stock, M.L. Passive mode locking by using nonlinear polarization evolution in a polarization-maintaining erbium-doped fiber. *Opt. Lett.* **1993**, *18*, 894–896. [[PubMed](#)]
22. Szczepanek, J.; Kardaš, T.M.; Radzewicz, C.; Stepanenko, Y. Ultrafast laser mode-locked using nonlinear polarization evolution in polarization maintaining fibers. *Opt. Lett.* **2017**, *42*, 575–578. [[CrossRef](#)]

23. Ilday, F.Ö.; Wise, F.W.; Sosnowski, T. High-energy femtosecond stretched-pulse fiber laser with a nonlinear optical loop mirror. *Opt. Lett.* **2002**, *27*, 1531–1533. [[CrossRef](#)]
24. Jiang, T.; Cui, Y.; Lu, P.; Li, C.; Wang, A.; Zhang, Z. All PM fiber laser mode locked with a compact phase biased amplifier loop mirror. *IEEE Photonics Technol. Lett.* **2016**, *28*, 1786–1789.
25. Yoshimi, H.; Sumimura, K.; Ozeki, Y. An er fiber laser generating multi-milliwatt picosecond pulses with ultralow intensity noise. *Jpn. J. Appl. Phys.* **2018**, *57*, 108001.
26. Zhou, J.; Pan, W.; Fu, X.; Zhang, L.; Feng, Y. Environmentally-stable 50-fs pulse generation directly from an Er: Fiber oscillator. *Opt. Fiber Technol.* **2019**, *52*, 101963.
27. Ma, Y.; Xu, B.; Ishii, H.; Meng, F.; Nakajima, Y.; Matsushima, I.; Schibli, T.R.; Zhang, Z.; Minoshima, K. Low-noise 750 MHz spaced ytterbium fiber frequency combs. *Opt. Lett.* **2018**, *43*, 4136–4139.
28. Ma, Y.; Salman, S.H.; Li, C.; Mahnke, C.; Hua, Y.; Droste, S.; Fellingner, J.; Mayer, A.S.; Heckl, O.H. Compact, all-PM fiber integrated and alignment-free ultrafast Yb: fiber NALM laser with sub-femtosecond timing jitter. *J. Light. Technol.* **2021**, *39*, 4431–4438. [[CrossRef](#)]
29. Lezius, M.; Wilken, T.; Deutsch, C.; Giunta, M.; Mandel, O.; Thaller, A.; Schkolnik, V.; Schiemangk, M.; Dinkelaker, A.; Kohfeldt, A.; et al. Space-borne frequency comb metrology. *Optica* **2016**, *3*, 1381–1387. [[CrossRef](#)]
30. Mayer, A.S.; Grosinger, W.; Fellingner, J.; Winkler, G.; Perner, L.W.; Droste, S.; Salman, S.H.; Li, C.; Heyl, C.M.; Heckl, O.H. Flexible all-PM NALM Yb: Fiber laser design for frequency comb applications: Operation regimes and their noise properties. *Opt. Express* **2020**, *28*, 18946–18968. [[CrossRef](#)]
31. Duan, D.; Wang, J.; Wu, Y.; Ma, J.; Mao, Q. Approach to high pulse energy emission of the self-starting mode-locked figure-9 fiber laser. *Opt. Express* **2020**, *28*, 33603–33613. [[CrossRef](#)] [[PubMed](#)]
32. Komarov, A.; Leblond, H.; Sanchez, F. Multistability and hysteresis phenomena in passively mode-locked fiber lasers. *Phys. Rev. A* **2005**, *71*, 053809.
33. Kim, D.; Kwon, D.; Lee, B.; Kim, J. Polarization-maintaining nonlinear-amplifying-loop-mirror mode-locked fiber laser based on a 3×3 coupler. *Opt. Lett.* **2019**, *44*, 1068–1071. [[CrossRef](#)] [[PubMed](#)]
34. Łaszczych, Z.; Soboń, G. Dispersion management of a nonlinear amplifying loop mirror-based erbium-doped fiber laser. *Opt. Express* **2021**, *29*, 2690–2702.
35. Dudley, J.M.; Barry, L.P.; Harvey, J.D.; Thomson, M.D.; Thomsen, B.C.; Bollond, P.G.; Leonhardt, R. Complete characterization of ultrashort pulse sources at 1550 nm. *IEEE J. Quantum Electron.* **1999**, *35*, 441–450. [[CrossRef](#)]
36. Ryu, U.C.; Oh, K.; Shin, W.; Paek, U.C. Inherent enhancement of gain flatness and achievement of broad gain bandwidth in erbium-doped silica fiber amplifiers. *IEEE J. Quantum Electron.* **2002**, *38*, 149–161.
37. Sun, Z.; Popa, D.; Hasan, T.; Hasan, T.; Torrisi, F.; Wang, F.; Kelleher, E.; Travers, J.; Nicolosi, V.; Ferrari, A. A stable, wideband tunable, near transform-limited, graphene-mode-locked, ultrafast laser. *Nano Res.* **2010**, *3*, 653–660.

Disclaimer/Publisher’s Note: The statements, opinions and data contained in all publications are solely those of the individual author(s) and contributor(s) and not of MDPI and/or the editor(s). MDPI and/or the editor(s) disclaim responsibility for any injury to people or property resulting from any ideas, methods, instructions or products referred to in the content.